Directionality of light absorption and emission in representative fluorescent proteins

Jitka Myšková[a], Olga Rybakova[a,b], Jiří Brynda[a,c], Petro Khoroshyy[a,b], Alexey Bondar[a,b], and Josef Lazar[a,b,1]

[a]Institute of Organic Chemistry and Biochemistry, Czech Academy of Sciences, 16610 Prague 6, Czech Republic; [b]Institute of Microbiology, Czech Academy of Sciences, 37333 Nové Hrady, Czech Republic; and [c]Institute of Molecular Genetics, Czech Academy of Sciences, 14220 Prague 4, Czech Republic

Fluorescent molecules are like antennas: The rate at which they absorb light depends on their orientation with respect to the incoming light wave, and the apparent intensity of their emission depends on their orientation with respect to the observer. However, the directions along which the most important fluorescent molecules in biology, fluorescent proteins (FPs), absorb and emit light are generally not known. Our optical and X-ray investigations of FP crystals have now allowed us to determine the molecular orientations of the excitation and emission transition dipole moments in the FPs mTurquoise2, eGFP, and mCherry, and the photoconvertible FP mEos4b. Our results will allow using FP directionality in studies of molecular and biological processes, but also in development of novel bioengineering and bioelectronics applications.

fluorescent protein | transition dipole moment | polarization microscopy

Since their first use in biology (1), fluorescent proteins (FPs) have illuminated an ever-expanding range of molecular events in cells, tissues, and organisms (2). FP-based genetically encoded sensors, nowadays indispensable in biological research, utilize various FP properties and their sensitivity to changes in molecular conformation, pH, or proximity to other optically active molecules. Implicit in the function of many FP-based sensors, but often acknowledged only cursorily or not at all, is the directionality of FP optical properties. Although directionality is a fundamental property of FP molecules, on par with excitation and emission spectra or excited state lifetimes, it remains largely unexplored and unexploited. Although polarization-resolved microscopy of FP-based constructs has been used to obtain information on molecular mechanisms of yeast cell division (3), G protein signaling (4, 5), cell membrane voltage sensing (6), or nuclear pore organization (7), this information cannot be properly interpreted in terms of protein structure without accurate quantitative knowledge of FP directionality. Knowledge of FP directionality would also allow interpreting fluorescence resonant energy transfer (FRET) experiments (8) on a new level. Finally, knowledge of optical directionality of FPs should allow rational development of novel genetically encoded optical probes.

Directionality of light absorption and emission by fluorescent molecules is characterized by vectors: the excitation and emission transition dipole moment (xTDM and mTDM, respectively). Only very limited information on FP TDMs is available. Although an experimental determination of xTDM directions for the green FP (GFP) through absorption measurements of protein crystals has been attempted (9), the data interpretation contained flaws (10), and the data themselves reveal serious experimental errors. Vibrational dichroism measurements carried out on GFP solution yielded a value of $67 \pm 4°$ for the angle between the xTDM of the 400-nm excitation and the stretching vibration of the carbonyl group of the fluorophore (11). However, this orientation disagrees with published results of quantum mechanical (QM) calculations (12, 13). Although the synthetic fluorophore of the GFP has been experimentally investigated (14), it can adopt conformations not allowed within the GFP molecular framework. Thus, TDM directions in FPs remain largely uncertain. Here we present the results of our efforts to

determine the directions of TDMs of several representative FPs through a combination of optical measurements and X-ray diffraction observations of FP crystals.

Results

Molecular Structure of FP Crystals. Although crystals of FPs have, in the past, failed to yield TDM directions, FP crystals do exhibit anisotropic light absorption and emission (15). Combining results of optical measurements of FP crystals with knowledge of the crystal structures should (9), in principle, allow determining directions of TDMs within FP molecules. In order to investigate directionality of optical properties of representative FPs, we prepared and examined crystals of mTurquoise2 (16, 17), eGFP (18–20), mCherry (21, 22), and mEos4b (23, 24) (a green-to-red photoconvertible FP, compatible with electron microscopy matrices). The excitation and emission wavelengths of the investigated FPs span a large section of the visible spectrum, and the studied fluorophores are present in most commonly used FPs. Our X-ray crystallography measurements (Fig. 1 and *SI Appendix*, Table S1) revealed that mTurquoise2 and eGFP (which crystallized at pH 7.5 and 3.8) formed crystals similar to those published (16, 25–29), in the orthorhombic space group $P2_12_12_1$, containing molecules in four distinct symmetry-related orientations. The photoconvertible FP mEos4b also crystallized in the $P2_12_12_1$ space group, but in an arrangement distinct from both eGFP and mTurquoise2, as well as from that published (30). Crystals of mCherry, distinct from those published (31), were in the monoclinic $C121$ space group, which contains molecules in

Significance

Fluorescent proteins have been used extensively in many areas of life sciences. Many of their applications rely on their various biophysical properties, such as excitation and emission wavelengths, excited state lifetimes, or sensitivity to the molecular environment. One aspect of fluorescent proteins that has remained largely neglected is the directionality of their optical properties. In the present work, we describe our experimental determination of the directionality of light absorption and emission in several commonly used fluorescent proteins. Our findings improve our understanding of fundamental properties of fluorescent proteins, and expand the possibilities of development and applications of genetically encoded fluorescent probes.

BIOPHYSICS AND COMPUTATIONAL BIOLOGY

Fig. 1. Properties of FP crystals. (*Left* to *Right*) Crystal structure (crystallographic axes as indicated, corresponding to the shown crystal orientations); typical images of crystal transmittance and fluorescence (polarizations of excitation and fluorescence indicated; scale bar, 20 μm); a plot showing typical values of crystal transmittance (*T*) and fluorescence intensity (*F*) for different polarizations of excitation and emission, respectively; and a plot of log ratios of extinction coefficients $\log_2(\varepsilon_{\parallel}/\varepsilon_{\perp})$ and fluorescence intensities $\log_2(F_{\parallel}/F_{\perp})$ for polarizations parallel ($\parallel$) and perpendicular ($\perp$) to the long crystal axis. Mean values and 95% CIs are indicated. Differences between observed values were classified as statistically nonsignificant (ns, $P > 0.05$), statistically significant (*$P < 0.05$), and statistically highly significant (***$P < 0.001$). (*A*) mTurquoise2; (*B*) eGFP, pH 7.5; (*C*) eGFP pH 3.8; (*D*) mCherry; (*E*) mEos4b.

two symmetry-related orientations. Importantly, X-ray diffraction measurements also yielded information on orientations of the crystallographic unit cells with respect to the crystal surfaces (Fig. 1). Briefly, in crystals of the $P2_12_12_1$ space group (mTurquoise2, eGFP, mEos4b), the long axis of the elongated crystals coincided with the

crystallographic axis A, while the major surfaces of the crystals bisected diagonally the rectangle outlined by the axes B, C. In crystals of the *C*121 space group (mCherry), the plane of the largely planar crystals corresponded to the AB plane of the crystal unit cell, with A corresponding to the long axis of the crystals.

Anisotropic Optical Properties of FP Crystals. Optical properties of FP crystals, positioned flat between two glass coverslips, were measured on a customized laser scanning confocal microscope (*SI Appendix*, Fig. S1). Although the crystals were conspicuously fluorescent, in order to determine orientations of xTDMs, we generally imaged absorption of the illuminating laser light as a function of the laser light polarization. Imaging absorption, rather than fluorescence, allowed avoiding artifacts caused by high concentration of the FP molecules in the crystals. An exception was made for the red form of mEos4b. Here, we used fluorescence intensity as a proxy for absorbance, in order to circumvent effects of absorbing but nonfluorescent side products of the green-to-red photoconversion. Conveniently, effects of high optical density could, in this case, be avoided by limiting photoconversion, thus lowering the concentration of the investigated species. In order to ascertain the directions of mTDMs, we measured polarization of the emitted fluorescence in all examined FPs. Our measurements revealed pronounced anisotropic optical properties in all of the investigated crystals (Fig. 1).

The observed optical properties of FP crystals were quantitated and interpreted in terms of TDM orientations. In order to derive the orientations of xTDMs, we ascertained the log ratios of extinction coefficients for light polarized parallel ($\varepsilon_\parallel$) and perpendicular ($\varepsilon_\perp$) to the long crystal axis (Table 1, Fig. 1, and *SI Appendix, Supplementary Text*). Analogously, we characterized the observed fluorescence polarization by log ratios of intensities of fluorescence polarized parallel ($F_\parallel$) and perpendicular ($F_\perp$) to the crystal long axis. The experimentally determined values of $\log_2(\varepsilon_\parallel/\varepsilon_\perp)$ and $\log_2(F_\parallel/F_\perp)$ were then compared to a mathematical model (*SI Appendix, Supplementary Text* and Fig. S3), based solely on two assumptions: 1) the TDM vector lying within the plane of the fluorophore and 2) a $\cos^2$ relationship between the TDM orientation and the observed optical property (absorption rate or fluorescence intensity). The model accounted for multiple molecular orientations present due to crystallographic symmetry. TDM orientations within a fluorophore were described by an angle (τ) between the TDM and a line connecting the centers of two aromatic rings of the fluorophore. For each crystal type, the model yielded a pair of orientations (τ_1, τ_2) consistent with the observed values of $\log_2(\varepsilon_\parallel/\varepsilon_\perp)$ or $\log_2(F_\parallel/F_\perp)$ (Fig. 2, *SI Appendix*, Fig. S3, and Table 1).

Distinguishing within Pairs of Possible TDM Orientations. In order to determine which one of the τ_1, τ_2 values (from now on denoted as τ_1) consistent with our measurements represented the TDM orientation, additional information was needed. The xTDMs were disambiguated by observations of FP crystals rotated along their long axis, and comparisons to mathematical model predictions (*SI Appendix*, Fig. S4). Disambiguation of mTDM determinations was carried out through measurements of fluorescence anisotropy (FA) of FP solutions (*SI Appendix*, Fig. S5). The observed FA allowed calculating the angle (β) between the absorbing and emitting dipoles (Table 1). The values of β ranged from slightly over 10° (mTurquoise2, 488-nm absorption of eGFP) to more than 15° (mCherry, green form of mEos4b). These β values are consistent with those published (32, 33). However, they are significantly higher than the differences between the mean xTDM and mTDM orientations within the fluorophore ($\Delta\tau_1$; $\Delta\tau_1 = |\tau_1(\text{mTDM}) - \tau_1(\text{xTDM})|$) determined by our crystal observations. Values of β, measured in FP solutions, include contributions of rotational diffusion and fluorophore vibrations, which have been shown, under conditions used in our FA measurements (34), to impart an apparent rotation of ~10° to FP molecules during their excited state lifetime. Thus, a β value of 10° (measured in FP solution) is consistent with $\Delta\tau_1$ close to 0° (measured in a crystal). The observed β values indicate that, within each pair of possible mTDM orientations (τ_1, τ_2), the one closer to the xTDM represents the true mTDM orientation within the fluorophore. This approach has now allowed us to unambiguously determine the xTDM and mTDM orientations in all of the studied FPs (Figs. 2 and 3, Table 1, and *SI Appendix*, Table S4).

Discussion

The TDM orientations derived from our experiments are, as expected, generally close to parallel to the long axis of the fluorophore, although sometimes with significant deviations. Observations of crystals of mTurquoise2 yield virtually identical xTDMs and mTDM orientations, in agreement with our FA measurements. In eGFP, crystal measurements reveal a subtle difference in orientation between xTDMs of the neutral and anionic forms, consistent with our FA observations, as well as with the known excited state proton transfer process in eGFP (14). Although the TDM directions in eGFP derived by us ($\tau_1 = 10.7° \pm 1.9°$) deviate significantly from the published QM predictions

Table 1. Results of optical measurements

FP	Wavelength (nm)	Log$_2$($\varepsilon_\parallel/\varepsilon_\perp$) or Log$_2$($F_\parallel/F_\perp$)) (±2 SEM)	τ_1 (95% CI)		N	β (±2 SEM)
mTurquoise2	405 (exc.)	2.42 ± 0.09	3.6°	(2.0° to 5.0°)	12	11.4° ± 0.4°
	458 (exc.)	2.39 ± 0.10	3.9°	(2.2° to 5.6°)	11	10.8° ± 0.2°
	489 to 531 (em.)	2.43 ± 0.07	3.4°	(2.0° to 4.7°)	10	
eGFP (pH 7.5)	405 (exc.)	2.53 ± 0.13	10.7°	(8.7° to 12.5°)	25	15.0° ± 0.2°
	488 (exc.)	2.34 ± 0.09	14.1°	(12.8° to 15.3°)	13	11.0° ± 0.1°
	529 to 555 (em.)	2.62 ± 0.12	12.6°	(9.6° to 15.3°)	18	
eGFP (pH 3.8)	405 (exc.)	2.63 ± 0.14	9.0°	(5.4° to 11.8°)	11	15.0° ± 0.2°
	488 (exc.)	2.29 ± 0.06	15.4°	(14.3° to 16.4°)	39	11.0° ± 0.1°
	529 to 555 (em.)	2.28 ± 0.08	15.5°	(14.2° to 16.8°)	15	
mCherry	543 (exc.)	0.32 ± 0.18	−7.5°	(−9.2° to −5.8°)	12	17.3° ± 0.1°
	594 (exc.)	0.48 ± 0.15	−8.7°	(−10.4° to −7.0°)	12	16.8° ± 0.1°
	600 to 690 (em.)	1.51 ± 0.12	−17.8°	(−18.6° to −16.9°)	12	
mEos4b (green form)	488 (exc.)	4.57 ± 0.13	−2.7°	(−3.6° to −1.8°)	13	13.0° ± 0.2°
	529 to 555 (em.)	3.89 ± 0.12	−7.4°	(−9.0° to −5.8°)	13	
mEos4b (red form)	594 (exc.)	3.25 ± 0.10	−12.6°	(−13.5° to −11.8°)	15	12.4° ± 1.3°
	600 to 690 (em.)	2.49 ± 0.13	−19.5°	(−20.7° to −18.4°)	12	

Log$_2$($\varepsilon_\parallel/\varepsilon_\perp$), log ratios of extinction coefficients of light polarized parallel and perpendicular to the long axis of the crystal; Log$_2$($F_\parallel/F_\perp$), log ratios of fluorescence intensities polarized parallel and perpendicular to the long axis of the observed crystals; τ_1, angle of the TDM with respect to the line connecting the centers of the fluorophore aromatic rings; N, number of crystals used for measurements; β, angle between the xTDM and mTDM, determined from FA measurements of FP solutions. Wavelengths used for investigating fluorescence excitation and emission marked (exc. and em., respectively).
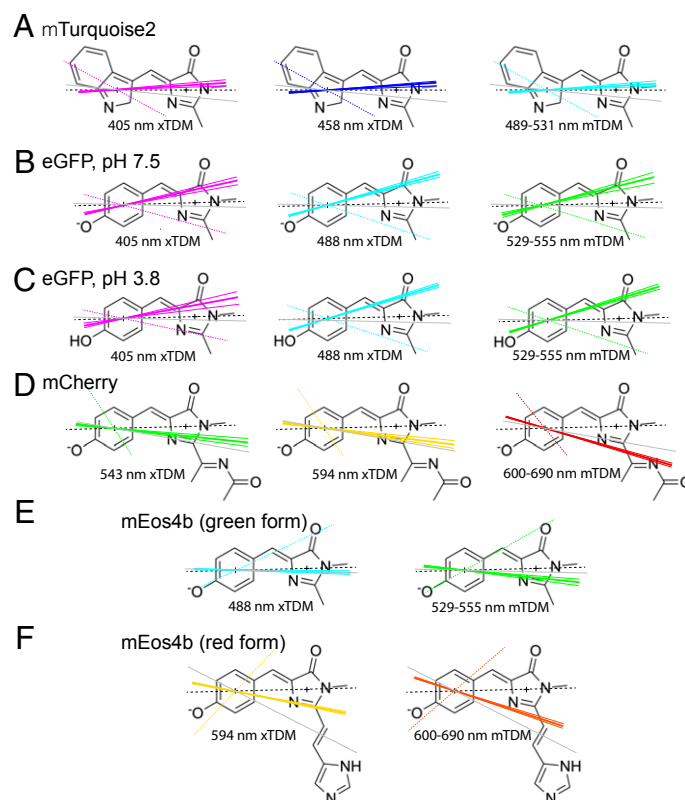
Fig. 2. Directions of TDMs within FP fluorophores. Full colored lines: means and 95% CIs of τ_1; dotted colored lines: directions τ_2, consistent with some but not all of our observations; thin gray lines: published QM predictions of TDM orientations. (*A*) mTurquoise2; (*B*) eGFP, pH 7.5; (*C*) eGFP, pH 3.8; (*D*) mCherry; (*E*) mEos4b (green form); (*F*) mEos4b (red form).

(12), they are in excellent agreement with the only other experimentally determined TDM direction (10, 11) (which corresponds to $\tau_1 = 10.3° \pm 4.0°$). The TDM orientations in mCherry reflect the extended conjugated double bond system of the fluorophore, and match the published QM predictions well. Surprisingly, the TDM orientations in the green form of mEos4b are distinct from those in the chemically identical fluorophore of eGFP. We attribute this to the conformational strain present in the mEos4b fluorophore (*SI Appendix*, Fig. S6). Although presence of multiple fluorophore states could also cause a similar result, neither our X-ray crystallography observations nor our spectroscopic measurements corroborate it.

Overall, our crystal measurements and FA observations have yielded a consistent set of xTDM and mTDM orientations, spanning an interval larger than 40° with respect to the FP β-barrel (Fig. 3). Variations in the conjugated double bond system of the fluorophore generally affect the TDM direction in an expected fashion. Dissociation of the phenolic OH group in GFP fluorophore changes the TDM orientation by ~3° toward the dissociated OH group. The observed trends are consistent with a close relationship between orientations of the TDM and the permanent dipole moment of the fluorophore.

Our approach entails separate determinations of xTDM orientations and mTDM orientations, and of the angle between them, and should be capable of identifying potential problems. However, our results are remarkably consistent, yielding credibility to our experimental approach. Although our work combines data acquired at cryogenic temperatures (X-ray crystallography) and at room temperature (polarization microscopy), the effects of the temperature difference are likely small, since published FP structures solved at room temperature (35) and at cryogenic temperatures (36, 37) differ in fluorophore orientation by less than 1°.

Similarly, comparing various available cryogenic X-ray structures (including ours) of the investigated FPs, often with distinct crystallization buffers and molecular crystal contacts, reveals variations in fluorophore orientation of only ~1°. We therefore estimate the accuracy of our determinations to be 1° to 2°.

We see two aspects of our work as critical for successful determination of molecular TDM orientations: detailed knowledge of the structure of the investigated crystals and thorough understanding of the relevant optical processes. Incorrect assumptions regarding crystallographic unit cell structure and orientation affected previous interpretations of FP crystal observations (9, 15). We caution against considering FP crystals as an "oriented gas" of isolated fluorophores (15), as the average distance between neighboring fluorophores is only around 4 nm, likely within the Förster radius for homoFRET. The high optical density of FP crystals leads to fluorescence reabsorption/reemission. These phenomena, along with unequal penetration depths of excitation light of distinct polarizations, prevent using fluorescence (and necessitate using absorption) for obtaining information on xTDMs in FP crystals. In contrast, by ensuring equal distribution of excitation among the multiple molecular orientations present, these phenomena aid in determinations of mTDM orientations through observations of fluorescence polarization in the trans direction. An even distribution of excitation is further supported by using excitation light polarized linearly along one of the axes of crystallographic symmetry (as light polarized circularly would cause uneven excitation of the distinct molecular orientations). Importantly, the impact of other phenomena on our experiments was limited. For example, observing crystals submerged in mother liquor containing polyethylene glycol (PEG) mitigated effects of differences in refractive indices, as shown by the agreement between our predictions and measurements of tilted crystal properties.
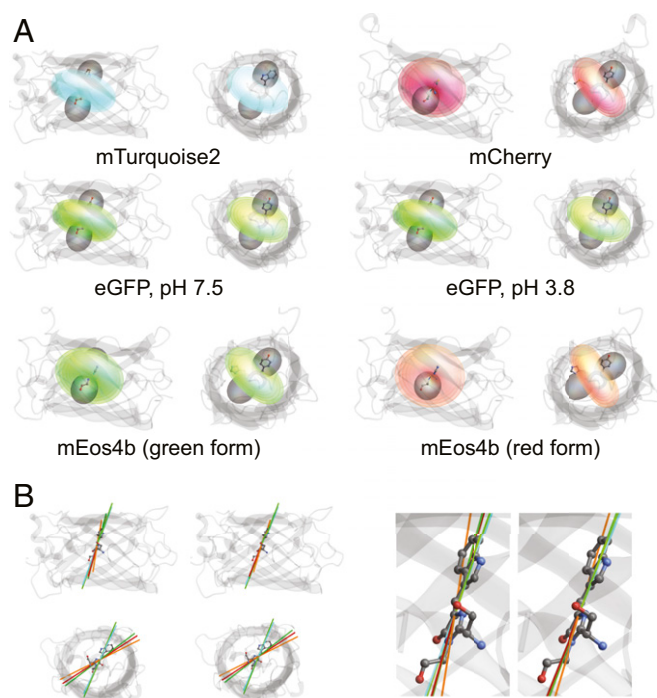
Fig. 3. Directionality of absorption and emission of FP molecules. (*A*) Radial plots of probabilities of light absorption for different polarizations (dark lobes), and of light emission for different emission directions (colored toroidal shapes), within the framework of the respective FP molecules, viewed laterally and axially. (*B*) Directions of xTDMs of the investigated FPs, after alignment to the structure of mTurquoise2 shown in stereo, for mTurquoise2 (in turquoise color), eGFP (light green), mCherry (dark red), and the green and red forms of mEos4b (dark green and orange, respectively).

No effects of crystal birefringence (double images; deviations of transmittance curves from $\cos^2$ shapes) were noticed, likely because the fast and slow refractive indices of protein crystals typically differ only by around 0.001 (38, 39). Using ratios (and log ratios) of extinction coefficients instead of the coefficients themselves allowed bypassing imprecisions in determinations of crystal thickness, as well as effects of small pH variations between crystal preparations.

Our results firmly establish FPs as directional light absorbers and emitters. Our findings will allow improved interpretations of FRET measurements and polarization microscopy observations, using existing (5, 40, 41) or newly developed software tools. They will be utilized in single-molecule and superresolution microscopy, particularly in cryogenic settings (such as in combination with cryoelectron microscopy), where low temperature greatly delays bleaching. Knowledge of FP directionality will also enable novel FP applications, such as in biological lasers (42) and bioelectronics (43). Some of those applications will likely take advantage of the possibility of isomorphic, yet directionally distinct, molecular replacements (mTurquoise2/eGFP, green/red forms of mEos4b). Furthermore, our results will inform future QM calculations of electronic and optical properties of molecules. We look forward to seeing the applications of our results.

Materials and Methods

Protein Purification and Crystallization. Plasmids were obtained as kind gifts from the laboratories of R. Campbell, University of Alberta, Edmonton, Canada (eGFP), D. Gadella, Univeristy of Amsterdam, Amsterdam, Holland (mTurquoise2), and R. Tsien, University of California, San Diego (mCherry), or synthesized commercially (mEos4b). FPs were expressed in *Escherichia coli*

(strain BL21, 200-mL cultures), and harvested after induction by isopropyl β-d-1-thiogalactopyranoside (IPTG). Cells were lysed by French press, and the lysate was cleared by ultracentrifugation and loaded onto a 1-mL His-Trap column (GE Healthcare). Fast protein liquid chromatography (ÄKTA, GE Healthcare) fractions were collected during elution with a 10- to 500-mM gradient of imidazole in a 200-mM NaCl, 50-mM Tris·HCl (pH 7.4) buffer. Fluorescent fractions were analyzed by sodium dodecyl sulfate polyacrylamide gel electrophoresis. Fractions containing highly pure protein were pooled, and concentrated by ultrafiltration (Vivaspin 10-kDa columns, Sartorius). Crystals were grown in hanging drops, by vapor diffusion at 18 °C, as follows: mTurquoise2 (1 μL of 6 to 10 mg/mL) with 2 μL of the well solution (14% PEG 8000, 100 mM Hepes pH 8.0 to 8.5, 80 mM MgCl₂) gave rise to crystals in the $P2_12_12_1$ space group; eGFP, 5 μL of 7 mg/mL solution with 2 μL of the well solution (20% PEG 8000, 50 mM KH₂PO₄ pH 3.8), and 2 μL of 10 to 15 mg/mL with 2 μL of the well solution (17% PEG 8000, 100 mM Hepes pH 7.5, 60 mM MgCl₂); mCherry (1.5 μL of 7.5 mg/mL solution) with 2 μL of 70% well solution C2 of the JCSG++ screen (Jena Bioscience); and mEos4b (2 μL of 10 mg/mL solution) with 1.5 μL of well solution B9 of the JCSG++ screen. For X-ray measurements, crystals were mounted in a loop, flash frozen, and stored in liquid nitrogen until use. For polarization microscopy measurements, crystals were placed in a drop (5 μL) of mother liquor and sandwiched between glass coverslips sealed by an adhesive spacer (SecureSeal, Grace Biolabs). Measurements of crystals rotated along their long axis were performed by observing crystals positioned on the coverslip at an angle, because of interactions with other crystals.

X-ray Crystallography. Diffraction datasets for eGFP, mTurquoise2, and mCherry crystals were collected in-house, on a MicroMax-007 HF Microfocus X-ray generator with a VariMax VHF ArcSec optical system (Rigaku), an AFC11 partial four-axis goniometer (Rigaku), a PILATUS 300K detector (Dectris), and a Cryostream 800 cryocooling system (Oxford Cryosystems). Diffraction datasets for mEos4b crystals were collected at 100 K on the MX 14.1 beamline operated by the Joint Berlin MX-Laboratory at the Berlin Electron Storage Ring of the Society for Synchrotron Radiation (BESSY II) in Berlin-Adlershof, Germany (44). All diffraction datasets were processed using the XDS software package (45). The crystal parameters and data collection and refinement statistics are summarized in *SI Appendix*, Table S1. All FP structures were solved by molecular replacement with CCP4 Molrep (46, 47), using available structures of identical proteins. The initial models were refined through several cycles of manual building using Coot and automated refinement with the software package CCP4 REFMAC5 (48). Visualizations of structural data were performed in PyMOL (49) and Chimera (50). Atomic coordinates and structure factors were deposited in the Protein Data Bank (PDB) under the codes 6YLM, 6YLN, 6YLP, 6YLQ, and 6YLS.

Optical Measurements. Polarization microscopy measurements were performed on a modified laser scanning microscope Olympus FV1200 (*SI Appendix*, Fig. S1), observing at least 10 crystals of each kind. For assessment of crystal shape and orientation, image z stacks of 1-μm spacing were acquired using a 40× objective lens (UApoN 340W, 40×, numerical aperture (NA) 1.15, Olympus) and illumination wavelength at the edge of the absorption band of the observed FP, in order for the illumination to reach the full thickness of the crystal. For polarization microscopy measurements, the illuminating laser beams traveled through a Glan-laser polarizer and a 0.5-mm aperture prior to being steered into the laser scanning unit.

For xTDM determinations, the laser beams passed through a superachromatic half-wave plate (SAHWP05M-700, Thorlabs), mounted in a motorized rotating mount (PRM1/MZ8, Thorlabs), prior to entering an underfilled 10× lens (UPlanFLN 10×, NA 0.3, Olympus). Transmitted light was collected by a low NA (0.55) condenser, whose numerical aperture was reduced by an internal diaphragm to NA of ~0.15. Before entering a photomultiplier detector, the transmitted light passed through a wavelength-specific band-pass filter (FB405-10, FL457.9-10, FL488-10, FL543.5-10, FB590-10, all Thorlabs) and a diffuser. For the red form of mEos4b, fluorescence passing through an emission filter (FELH0600, Thorlabs) was detected (instead of transmitted laser light). During measurements, polarization of the laser beam was rotated between acquisition of individual images in 10° increments over the range of 0° to 720°. Small changes in excitation light intensity with polarization modulation were noted; however, they did not affect measurements of transmittance, as they applied equally to the crystal and background segments of the analyzed images.

For mTDM determinations, restricted diameter laser beam was scanned through a 10× lens (UPlanFLN 10×, NA 0.3, Olympus). In order to ensure equal excitation of all molecular orientations present in the crystal, the excitation light was polarized linearly, parallel to the long crystal axis. Fluorescence was collected by a low NA (0.55) condenser, whose numerical

aperture was reduced by an internal diaphragm to NA of ~0.15. Before entering a photomultiplier detector, the collected fluorescence passed through an emission filter (Brightline 510/42 for mTurquoise2, 542/27 for eGFP and mEos4b, FELH0600 for mCherry and mEos4b, all Thorlabs), a polarizer mounted in a motorized rotating mount, and a diffuser. During measurements, the polarizer was rotated between acquisition of individual images in 10° increments over the range of 0° to 720°. Polarization sensitivity of the detection pathway (4.6%) was compensated for during data analysis.

FA measurements were performed in 60% glycerol/50 mM Tris solutions of FPs (10 µg/mL) in a 1-cm quartz cuvette, at 22.5 °C (as in ref. 34), using the Horiba FluoroMax4 fluorometer equipped with calcite polarizer-based fluorescence polarization module (alignment precision better than 1°). Excitation and emission slits were set to 1 and 3 nm, respectively. Signal was integrated over 1 s to 4 s. Mean values and SEs were calculated from triplicate measurements.

Microscopy Image Analysis. Microscopy images were processed in Fiji, using publicly available tools and in-house developed macros. For xTDM determinations, the stacks of time series images acquired with different polarizations were precisely aligned by the StackReg plugin (51), and a dark detector response was subtracted. Images were then normalized by an intensity corresponding to unattenuated laser power, calculated from parts of the image not containing the crystal. The resulting transmittance images were manually segmented, and transmittance values of flat, clear parts of the observed crystals suitable for analysis were plotted as a function of polarization of the illuminating light. Values of transmittances of light polarized parallel and perpendicular to the long axis of crystal ($T_\parallel$, $T_\perp$) were obtained by fitting the transmitted light intensity data by a cosine squared function. $T_\parallel$ and $T_\perp$ were then used to derive the value of $\varepsilon_\parallel/\varepsilon_\perp$, (and $\log_2(\varepsilon_\parallel/\varepsilon_\perp)$), either using the simple relationship $\varepsilon_\parallel/\varepsilon_\perp = \log(T_\parallel/T_{\parallel 0})/\log(T_\perp/T_{\perp 0})$ (for light of wavelengths 543 and 594 nm, of polarization purity better than 99.8%), or a more complicated formula (*SI Appendix, Supplementary Text* and Table S2; for wavelengths of 405, 458, and 488 nm, whose polarization purity was lower than 99.8%). Using log ratios allowed applying Gaussian statistics (generally not suitable to ratios), as well as comparing the precision of determinations of $\varepsilon_\parallel/\varepsilon_\perp$ spanning a large range of values. To interpret measurements of tilted crystals, the extent of rotation about the crystal long axis (crystal roll angle) was determined in Fiji by applying the angle measurement tool to vertical cross-sections of z stacks of confocal images. Z-stack cross-sections also yielded information on crystal thickness, which (when combined with protein concentration derived from the X-ray structures) allowed calculation of the molar extinction coefficients $\varepsilon_\parallel$, $\varepsilon_\perp$ (*SI Appendix,* Table S3). However, only the $\varepsilon_\parallel/\varepsilon_\perp$ ratios, derived solely from transmitted light measurements, were used for xTDM determinations.

For mTDM determinations, images of fluorescence intensity, acquired in the trans direction, with different orientations of an analyzer placed in the detection pathway, were background subtracted and manually segmented. Fluorescence intensity was then plotted as a function of the analyzer orientation. Values of fluorescence intensities polarized parallel and perpendicular to the long axis of crystal ($F_\parallel$, $F_\perp$) and their log ratio ($\log_2(F_\parallel/F_\perp)$) were obtained by fitting the fluorescence intensity data by a cosine squared function.

Mathematical Modeling. The TDM directions with respect to the fluorophore were identified by mathematical modeling, using Mathematica (Wolfram Research). The fluorophore plane was defined by least-square fitting of coordinates of heavy atoms participating in the conjugated bond system (*SI Appendix,* Fig. S2). Optical measurements of the red form of mEos4b were interpreted using the published structure (PDB ID code 6GOY) aligned with the structure of the green form of mEos4b determined by us (6YLS). The TDM vector was postulated to lie within the fluorophore plane, at an angle τ with respect to a line connecting the centers of the fluorophore aromatic rings. For xTDM determinations, values of $\log_2(\varepsilon_\parallel/\varepsilon_\perp)$ expected for different values of τ (*SI Appendix,* Fig. S3) were calculated by using a $\cos^2$ relationship of the absorption rate on the angle between the polarization of the excitation light and the xTDMs present in the crystal. The $\log_2(\varepsilon_\parallel/\varepsilon_\perp)$ value derived from optical measurements was compared to the $\log_2(\varepsilon_\parallel/\varepsilon_\perp)$ predictions, yielding two xTDM orientations (values of τ) matching the results of crystal measurements. From the two τ values, the one consistent with measurements performed on tilted FP crystals (*SI Appendix,* Fig. S4) was taken to represent the TDM orientation (τ_1). An analogous procedure was used in mTDM orientation determinations, using intensities of fluorescence polarized parallel ($F_\parallel$) and perpendicular ($F_\perp$) to the long axis of crystal instead of extinction coefficients. In order to distinguish between the two τ values obtained from fluorescence polarization measurements, we used information on FA in FP solutions and directions of xTDMs.

Statistical Analysis. All optical measurements of FP crystals were carried out on at least 10 crystals, as indicated (Table 1). Mean values and 95% CIs (± 2 SEM) of values of $\log_2(\varepsilon_\parallel/\varepsilon_\perp)$ and $\log_2(F_\parallel/F_\perp)$ (Fig. 1 and Table 1) were used to calculate the means and 95% CIs of TDM orientations (angles τ) (Fig. 2 and Table 1). Unpaired t test was used to compare results of crystal measurements, and P value < 0.05 (marked by * in Fig. 1) was used as a statistical significance cutoff. P value < 0.001 is marked by ***. Measurements of FA were carried out in triplicates and mean values and 95% CIs (± 2 SEM) were calculated (Table 1 and *SI Appendix,* Fig. S5).

Data Availability. Protein structures data have been deposited in the PDB (PDB ID codes 6YLM (mCherry), 6YLN (mTurquoise2), 6YLQ (eGFP, pH 7.5), 6YLP (eGFP, pH 3.8) and 6YLS (mEos4b)).

1. M. Chalfie, Y. Tu, G. Euskirchen, W. W. Ward, D. C. Prasher, Green fluorescent protein as a marker for gene expression. *Science* **263**, 802–805 (1994).

2. E. C. Greenwald, S. Mehta, J. Zhang, Genetically encoded fluorescent biosensors illuminate the spatiotemporal regulation of signaling networks. *Chem. Rev.* **118**, 11707–11794 (2018).

3. A. M. Vrabioiu, T. J. Mitchison, Structural insights into yeast septin organization from polarized fluorescence microscopy. *Nature* **443**, 466–469 (2006).

4. A. Bondar, J. Lazar, The G protein G_{i1} exhibits basal coupling but not preassembly with G protein-coupled receptors. *J. Biol. Chem.* **292**, 9690–9698 (2017).

5. J. Lazar, A. Bondar, S. Timr, S. J. Firestein, Two-photon polarization microscopy reveals protein structure and function. *Nat. Methods* **8**, 684–690 (2011).

6. Z. Han *et al.*, Mechanistic studies of the genetically encoded fluorescent protein voltage probe ArcLight. *PLoS One* **9**, e113873 (2014).

7. M. Kampmann, C. E. Atkinson, A. L. Mattheyses, S. M. Simon, Mapping the orientation of nuclear pore proteins in living cells with polarized fluorescence microscopy. *Nat. Struct. Mol. Biol.* **18**, 643–649 (2011).

8. F. T. Chan, C. F. Kaminski, G. S. Kaminski Schierle, HomoFRET fluorescence anisotropy imaging as a tool to study molecular self-assembly in live cells. *ChemPhysChem* **12**, 500–509 (2011).

9. F. I. Rosell, S. G. Boxer, Polarized absorption spectra of green fluorescent protein single crystals: Transition dipole moment directions. *Biochemistry* **42**, 177–183 (2003).

10. X. Shi *et al.*, Anomalous negative fluorescence anisotropy in yellow fluorescent protein (YFP 10C): Quantitative analysis of FRET in YFP dimers. *Biochemistry* **46**, 14403–14417 (2007).

11. D. Stoner-Ma *et al.*, Proton relay reaction in green fluorescent protein (GFP): Polarization-resolved ultrafast vibrational spectroscopy of isotopically edited GFP. *J. Phys. Chem. B* **110**, 22009–22018 (2006).

12. T. Ansbacher *et al.*, Calculation of transition dipole moment in fluorescent proteins—Towards efficient energy transfer. *Phys. Chem. Chem. Phys.* **14**, 4109–4117 (2012).

13. M. Khrenova, I. Topol, J. Collins, A. Nemukhin, Estimating orientation factors in the FRET theory of fluorescent proteins: The TagRFP-KFP pair and beyond. *Biophys. J.* **108**, 126–132 (2015).

14. A. Usman *et al.*, Excited-state structure determination of the green fluorescent protein chromophore. *J. Am. Chem. Soc.* **127**, 11214–11215 (2005).

15. S. Inoué, O. Shimomura, M. Goda, M. Shribak, P. T. Tran, Fluorescence polarization of green fluorescence protein. *Proc. Natl. Acad. Sci. U.S.A.* **99**, 4272–4277 (2002).

16. J. Goedhart et al., Structure-guided evolution of cyan fluorescent proteins towards a quantum yield of 93%. Nat. Commun. 3, 751 (2012).

17. J. Myskova, M. Rybakova, J. Brynda, J. Lazar, mTurquoise2 SG P212121 - Directional optical properties of fluorescent proteins. Protein Data Bank. https://www.rcsb.org/structure/6YLN. Deposited 7 April 2020.

18. B. P. Cormack, R. H. Valdivia, S. Falkow, FACS-optimized mutants of the green fluorescent protein (GFP). Gene 173, 33–38 (1996).

19. J. Myskova, M. Rybakova, J. Brynda, J. Lazar, EGFP in neutral pH, Directionality of optical properties of fluorescent proteins. Protein Data Bank. https://www.rcsb.org/structure/unreleased/6YLQ. Deposited 7 April 2020.

20. J. Myskova, M. Rybakova, J. Brynda, J. Lazar, EGFP_in_Acidic_env directionality of optical properties of fluorescent proteins. Protein Data Bank. https://www.rcsb.org/structure/unreleased/6YLP. Deposited 7 April 2020.

21. N. C. Shaner et al., Improved monomeric red, orange and yellow fluorescent proteins derived from Discosoma sp. red fluorescent protein. Nat. Biotechnol. 22, 1567–1572 (2004).

22. J. Myskova, M. Rybakova, J. Brynda, J. Lazar, mCherry. Protein Data Bank. https://www.rcsb.org/structure/6YLM. Deposited 7 April 2020.

23. M. G. Paez-Segala et al., Fixation-resistant photoactivatable fluorescent proteins for CLEM. Nat. Methods 12, 215–218 (2015).

24. J. Myskova, M. Rybakova, J. Brynda, J. Lazar, mEos4b - Directionality of optical properties of fluorescent Proteins. Protein Data Bank. https://www.rcsb.org/structure/unreleased/6YLS. Deposited 7 April 2020.

25. M. Ormö et al., Crystal structure of the Aequorea victoria green fluorescent protein. Science 273, 1392–1395 (1996).

26. F. Yang, L. G. Moss, G. N. Phillips Jr, The molecular structure of green fluorescent protein. Nat. Biotechnol. 14, 1246–1251 (1996).

27. K. Brejc et al., Structural basis for dual excitation and photoisomerization of the Aequorea victoria green fluorescent protein. Proc. Natl. Acad. Sci. U.S.A. 94, 2306–2311 (1997).

28. A. Royant, M. Noirclerc-Savoye, Stabilizing role of glutamic acid 222 in the structure of enhanced green fluorescent protein. J. Struct. Biol. 174, 385–390 (2011).

29. J. A. Arpino, P. J. Rizkallah, D. D. Jones, Crystal structure of enhanced green fluorescent protein to 1.35 Å resolution reveals alternative conformations for Glu222. PLoS One 7, e47132 (2012).

30. E. De Zitter et al., Mechanistic investigation of mEos4b reveals a strategy to reduce track interruptions in sptPALM. Nat. Methods 16, 707–710 (2019).

31. X. Shu, N. C. Shaner, C. A. Yarbrough, R. Y. Tsien, S. J. Remington, Novel chromophores and buried charges control color in mFruits. Biochemistry 45, 9639–9647 (2006).

32. J. V. Rocheleau, M. Edidin, D. W. Piston, Intrasequence GFP in class I MHC molecules, a rigid probe for fluorescence anisotropy measurements of the membrane environment. Biophys. J. 84, 4078–4086 (2003).

33. A. Volkmer, V. Subramaniam, D. J. Birch, T. M. Jovin, One- and two-photon excited fluorescence lifetimes and anisotropy decays of green fluorescent proteins. Biophys. J. 78, 1589–1598 (2000).

34. M. Oura et al., Polarization-dependent fluorescence correlation spectroscopy for studying structural properties of proteins in living cell. Sci. Rep. 6, 31091 (2016).

35. G. Gotthard et al., Specific radiation damage is a lesser concern at room temperature. IUCrJ 6, 665–680 (2019).

36. G. Gotthard, D. von Stetten, D. Clavel, M. Noirclerc-Savoye, A. Royant, Chromophore isomer stabilization is critical to the efficient fluorescence of cyan fluorescent proteins. Biochemistry 56, 6418–6422 (2017).

37. M. Lelimousin et al., Intrinsic dynamics in ECFP and Cerulean control fluorescence quantum yield. Biochemistry 48, 10038–10046 (2009).

38. T. Ruiz, R. Oldenbourg, Birefringence of tropomyosin crystals. Biophys. J. 54, 17–24 (1988).

39. R. L. Owen, E. Garman, A new method for predetermining the diffraction quality of protein crystals: Using SOAP as a selection tool. Acta Crystallogr. D Biol. Crystallogr. 61, 130–140 (2005).

40. M. McQuilken et al., Polarized fluorescence microscopy to study cytoskeleton assembly and organization in live cells. Curr. Protocols Cell Biol. 67, 4.29.1–4.29.13 (2015).

41. K. Zhanghao et al., Super-resolution imaging of fluorescent dipoles via polarized structured illumination microscopy. Nat. Commun. 10, 4694 (2019).

42. M. C. Gather, S. H. Yun, Single-cell biological lasers. Nat. Photonics 5, 406–410 (2011).

43. R. A. Cinelli et al., Green fluorescent proteins as optically controllable elements in bioelectronics. Appl. Phys. Lett. 79, 3353–3355 (2001).

44. M. Gerlach, U. Mueller, M. S. Weiss, The MX beamlines BL14. 1-3 at BESSY II. J. Large-Scale Res. 2, 47 (2016).

45. W. Kabsch, Integration, scaling, space-group assignment and post-refinement. Acta Crystallogr. D Biol. Crystallogr. 66, 133–144 (2010).

46. M. D. Winn et al., Overview of the CCP4 suite and current developments. Acta Crystallogr. D Biol. Crystallogr. 67, 235–242 (2011).

47. A. Vagin, A. Teplyakov, Molecular replacement with MOLREP. Acta Crystallogr. D Biol. Crystallogr. 66, 22–25 (2010).

48. A. A. Vagin et al., REFMAC5 dictionary: Organization of prior chemical knowledge and guidelines for its use. Acta Crystallogr. D Biol. Crystallogr. 60, 2184–2195 (2004).

49. Schrodinger, The PyMOL Molecular Graphics System (Schrodinger LLC, 2010), Version 1.0.

50. E. Pettersen et al., UCSF Chimera—A visualization system for exploratory research and analysis. J. Comput. Chem. 223, 1605–1612 (2004).

51. P. Thévenaz, U. E. Ruttimann, M. Unser, A pyramid approach to subpixel registration based on intensity. IEEE Trans. Image Process. 7, 27–41 (1998).

BIOPHYSICS AND
COMPUTATIONAL BIOLOGY